

High-Throughput Growth of HfO₂ Films Using Temperature-gradient Laser Chemical Vapor Deposition

Rong TU

Wuhan University of Technology

Ziming LIU

Wuhan University of Technology

Chongjie WANG

Wuhan University of Technology

Pengjian LU

Wuhan University of Technology

Bingjian GUO

Wuhan University of Technology

Qingfang XU

Wuhan University of Technology

Bao-Wen LI

Wuhan University of Technology

Chuanbin WANG

Wuhan University of Technology

Lianmeng ZHANG

Wuhan University of Technology

Song Zhang (✉ kobe@whut.edu.cn)

Wuhan University of Technology

Research Article

Keywords: Laser chemical vapor deposition (LCVD), Temperature gradient, High-throughput growth, HfO₂ films, Microstructure, Growth mechanism

Posted Date: December 8th, 2021

DOI: <https://doi.org/10.21203/rs.3.rs-1127423/v1>

License:   This work is licensed under a Creative Commons Attribution 4.0 International License.

[Read Full License](#)

High-throughput growth of HfO₂ films using temperature-gradient laser chemical vapor deposition

Rong TU^{1, 2}, Ziming LIU², Chongjie WANG², Pengjian LU^{2, 3}, Bingjian GUO^{4, 5},
Qingfang XU², Bao-Wen LI⁴, Chuanbin WANG², Lianmeng ZHANG^{2, 1}, Song
ZHANG^{2, *}

¹ Chaozhou Branch of Chemistry and Chemical Engineering Guangdong Laboratory,
Chaozhou 521000, People's Republic of China

² State Key Laboratory of Advanced Technology for Materials and Processing, Wuhan
University of Technology, 122 Luoshi Road, Wuhan 430070, People's Republic of
China

³ Wuhan Tuocai Technology Co., Ltd., 147 Luoshi Road, Wuhan 430070, People's
Republic of China

⁴ School of Materials Science and Engineering, Wuhan University of Technology, 122
Luoshi Road, Wuhan 430070, People's Republic of China

⁵ Zhejiang MTCN Technology Co., Ltd. No. 59, Luhui Road, Taihu street, Zhejiang
Province 311103, People's Republic of China

*Corresponding author, Song ZHANG: Tel/Fax: +86-27-87499449;

E-mail: kobe@whut.edu.cn

Abstract: The use of hafnia (HfO_2) has facilitated recent advances in combining uprated dielectric layers (UDLs) and environmental barriers (EBs) in supercomputers. However, an extremely low deposition rate limits further development and fabrication efficiency of HfO_2 films. In this study, high-throughput growth of HfO_2 films was realized via laser chemical vapor deposition using a laser spot with a gradient temperature distribution. In HfO_2 films fabricated by a single growth process, four regions with different morphologies could be discerned for deposition temperatures increasing from 1300 K to 1600 K: *leaf-like*, *pyramid-like*, *bromeliad-like* and *pinecone-like*. Two growth modes were observed for Regions I and II: Stranski-Krastanov and Volmer-Weber. Regions III and IV contained coexisting monoclinic and tetragonal HfO_2 grains with an in-plane boundary for m- HfO_2 (-110) $\{111\}$ //t- HfO_2 (1-11) $\{111\}$. The maximum deposition rate reached 362 $\mu\text{m}/\text{h}$, which was $10^2 - 10^4$ times higher than that obtained using existing deposition methods.

Key words: Laser chemical vapor deposition (LCVD); Temperature gradient; High-throughput growth; HfO_2 films; Microstructure; Growth mechanism.

1. Introduction

Supercomputers based on a combination of uprated dielectric layers (UDLs) and environmental barriers (EBs) offer the advantages of a compact size, adaptive integration, and massive parallelization [1]. Thus, corresponding advances are required in dielectric materials to passivate exposed surfaces against destabilization related to ion transport [2] and in barrier materials to protect core components against thermal shock or fluid erosion in harsh operating environments [3]. Processing studies have

shown that a traditional SiO₂ barrier layer with a thickness of over 50 μm sustained a weight loss of more than 70% after 500 cycles in a thermal-shock test [4], which does not meet the requirements of miniaturization and sustainability. In 2007, Intel *Inc.* announced that HfO₂, a high-k inorganic material with an ultrahigh melting point (3085 K) [5], a sufficient electrical breakdown field (3.9–6.7 MV/cm) [6], low thermal conductivity (~2.55 W·K⁻¹·m⁻¹), and four times the density (9.68 g/cm³) of SiO₂ (2.26 g/cm³) [7], as the most promising dielectric layer material to replace the traditional SiO₂ layer for a new generation of supercomputers [8].

Table 1. Comparison of deposition temperatures and rates of HfO₂ films grown using different methods.

Ref.	Method	Precursor	T_{dep} (K)	R_{dep} (μm/h)
[9]	MOCVD	Cp ₂ Hf(NEt ₂) ₂	1273	2.40 × 10 ⁻¹
[10]	MOCVD	(Cp ₂ CMe ₂)HfMe ₂	923	7.20 × 10 ⁻²
[11]	MOCVD	Hf(dmml) ₄	973	5.40 × 10 ⁻²
[12]	TCVD	HfCl ₄	473	1.64 × 10 ⁻³
[13]	ALD	Hf(NMe ₂) ₄	1373	9.60 × 10 ⁻³
[14]	ALD	HfO ^t Bu(NEtMe) ₃	623	8.90 × 10 ⁻²
[15]	ALD	Hf(NEtMe) ₄	633	1.01 × 10 ⁻¹
[16]	ALD	Hf(NMe ₂) ₄	1273	8.64 × 10 ⁻²
[17]	ALD	CpHf(NMe ₂) ₃	523	7.20 × 10 ⁻²
[18]	sol-gel	HfCl ₄	873	1.03 × 10 ⁻³
[19]	sol-gel	HfCl ₄	823	2.07 × 10 ⁻³
[20]	sol-gel	HfCl ₄	873	6.67 × 10 ⁻³
[21]	RFMS	HfO ₂ target	573	7.50 × 10 ⁻²
[22]	PLD	HfO ₂ target	1173	8.52 × 10 ⁻¹
This study	HT-LCVD	Hf(acac) ₄	1300~1600	4.68 × 10 ⁻¹ ~ 3.62 × 10 ⁻²

Table 1 shows the deposition temperature (T_{dep}) and deposition rate (R_{dep}) measured for HfO₂ films grown using different methods, such as metal-organic CVD (MOCVD) [9-11], thermal CVD (TCVD) [12], atomic layer deposition (ALD) [13-17], sol-gel [18-20], radio frequency magnetron sputtering (RFMS) [21] and pulsed laser deposition (PLD) [22]. As a result of the extremely low deposition rate of HfO₂ films, only a few scholars have studied the growth of films with thicknesses below 100 nm over the last decade, such that HfO₂ films have not been exploited at the micron scale. Since 2012, our group has been developing LCVD [23] to significantly improve the CVD deposition rates, and we have been able to rapidly grow SiC [24], SiOC [25], AlN [26], LiAlO₂ [27], BaTi₂O₅ [28], and SmBa₂Cu₃O₇ [29] films at deposition rates 10-10⁴ times higher than those of conventional CVD methods. Novel structures and growth mechanisms have been found using LCVD to grow films [30].

High-throughput growth offers a significant advantage toward improving the experimental efficiency in that multiple specimens are obtained from a single preparation. Advances in CVD need to be made to realize high-throughput growth, which is currently mainly achieved using physical vapor deposition (PVD) because of good uniformity, excellent step coverage, simple equipment, and convenient control of the film composition [31]. However, various factors in CVD processes, such as the growth temperature, pressures, and gas flow rates, need to be further investigated [32]. The presence of multiple variables and uncertainties in these variables result in an extended experimental time and deteriorate the repeatability of the entire process; hence, little pertinent research has been performed on high-throughput CVD.

We significantly shortened the experimental time by modifying the high-throughput LCVD (HT-LCVD) method by using a temperature-gradient preparation with credible measurement and repeatability, resulting in $10^2 - 10^4$ times higher growth rates than other methods and the fabrication of multiple specimens per unit time. In this study, HfO₂ films were grown using a highly efficient HT-LCVD process. The morphologies, deposition rates and growth mechanisms of four novel microstructures were determined.

2. Experimental Section

[Fig. 1](#) shows the HT-LCVD apparatus that was constructed to fabricate HfO₂ films. An InGaAlAs beam-by-diode laser (wavelength: 808 nm, LHTC-200, ZK-LASER, China) was introduced into the chamber through a quartz-glass window and diverged by an optical lens (around 18 mm in diameter) to irradiate the entire substrate surface. The diode laser beam created a temperature-gradient distribution over the substrate surface. [Fig. 2](#) shows vertical and stereo views of the temperature distribution during high-throughput growth. As T_{dep} increased from 1300 K to 1600 K, four specific regions with different novel microstructures could be observed for several specimens fabricated by a single growth process. The temperature distribution was measured by an infrared pyrometer (CHINO IR-AH) and regulated by an infrared temperature-measurement program (OMRON, Japan). [Fig. 3](#) shows the growth procedure. Si (100) single crystal wafers were cut into samples with dimensions of $10.0 \times 10.0 \times 0.5$ mm for use as substrates, which were placed on a heating stage in the chamber and preheated at 873 K for 5 min after evacuating the chamber to 5 Pa. The substrate holder was supported

by an alumina plate with a K-type thermocouple, which was used to monitor the temperature of the heating stage. The precursor, $\text{Hf}(\text{acac})_4$ (Aladdin Inc., Shanghai, China), was vaporized at 493 K and carried into the vacuum chamber by Ar gas (99.999%). [Table 2](#) shows a summarization of deposition conditions used to prepare the temperature-gradient HfO_2 films via HT-LCVD.

The crystalline phases were examined by the microarea X-ray diffraction (μ -XRD; D8 DISCOVER, Bruker, Germany; 40 kV, 40 mA) with Cu $K\alpha_2$ radiation, whereby a small region (0.4 mm in diameter) in the specimen was fingerprinted. The composition of the microarea on the surface was detected by Raman spectroscopy (inVia, Renishaw, 633 nm He-Ne laser, UK). The surface and cross-section morphologies were characterized by scanning electron microscopy (SEM, Quanta FEG 450, FEI, USA, at 20 kV). The microstructures were observed using double-beam electron microscopy with focused ion beam processing (FIB, Helios NanoLab G3 UC, FEI, USA, at 20 kV) and transmission electron microscopy (TEM, JEOL Ltd., Japan, JEM-2100F, at 200 kV).

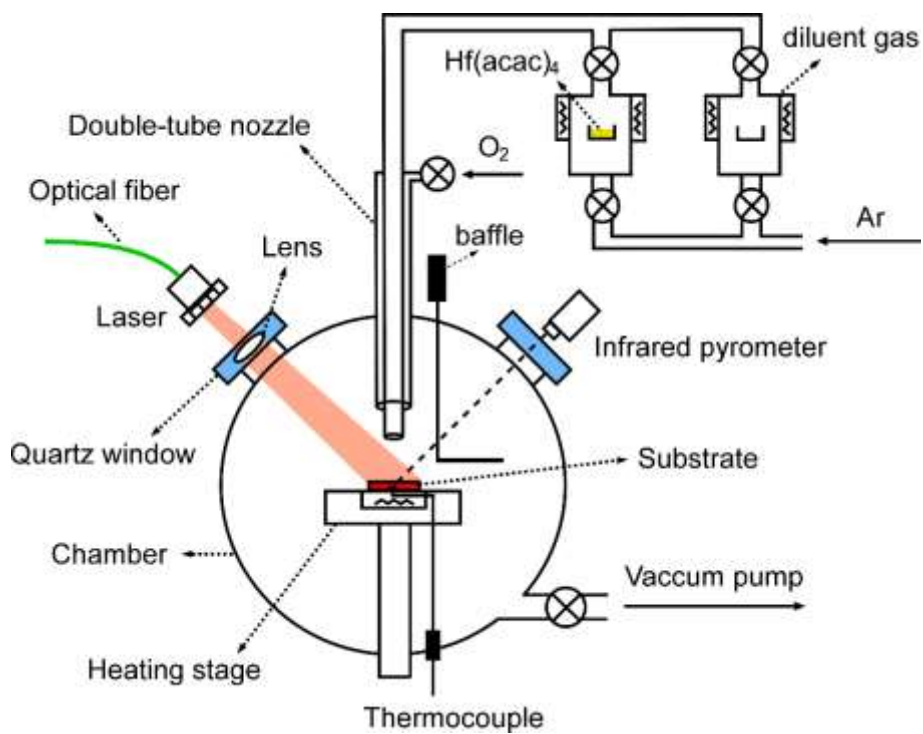


Fig. 1. Schematic of the HT-LCVD apparatus.

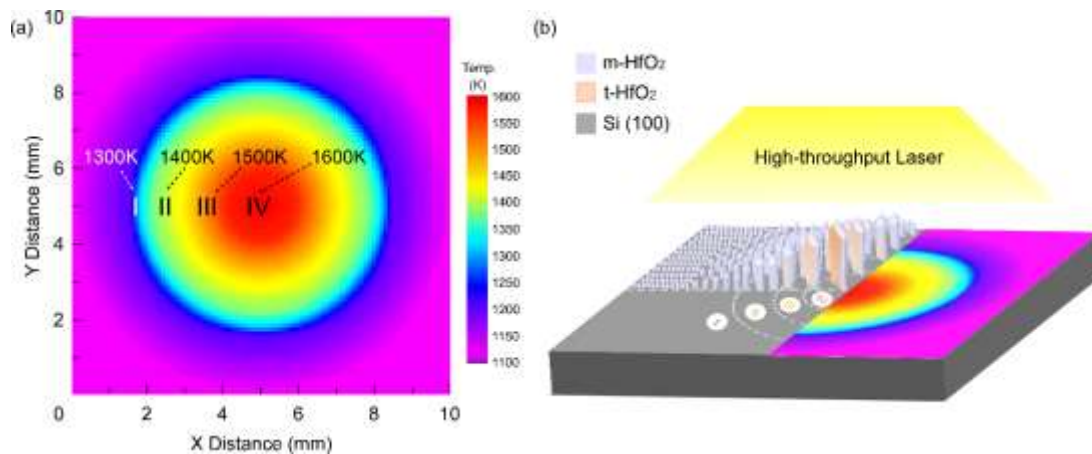


Fig. 2. (a) Top view of the temperature distribution and (b) stereo view of four discernible regions.

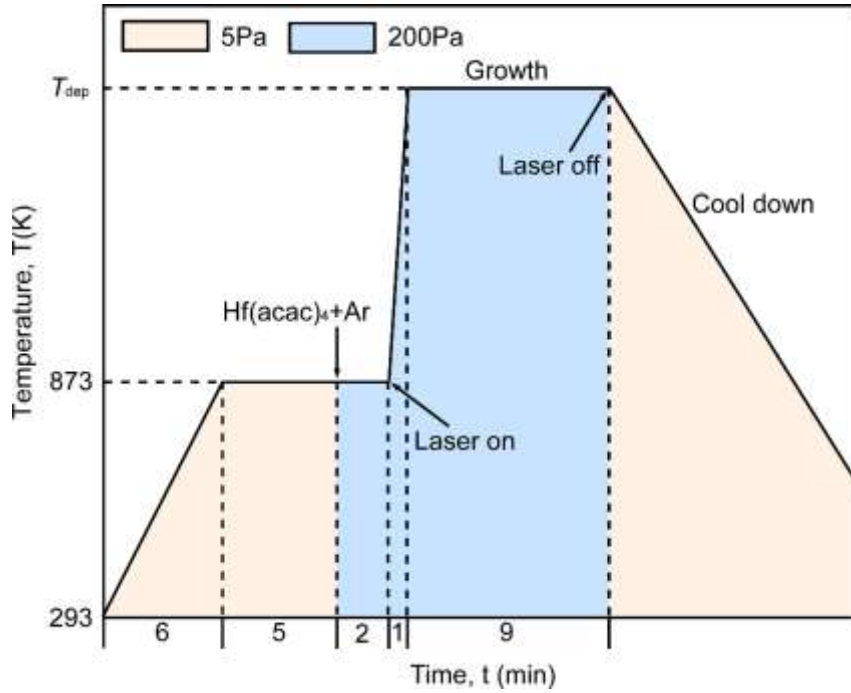


Fig. 3. Diagram showing the evolution of temperature in HfO₂ films grown using HT-LCVD.

Table 2. Deposition Conditions

Precursor:	Hf(acac) ₄
Substrate:	Si (100)
Deposition temperature (T_{dep}):	1250-1600 K
Total pressure (P_{tot}):	200 Pa
Laser power (P_L):	100 W
Precursor vaporization temperature:	493 K
Pipe/gas nozzle temperature (T_{pip}):	573K
Deposition time (t_{dep}):	10 min
Ar carrier gas flow rate:	$1.67 \times 10^{-6} \text{ m}^3 \text{ s}^{-1}$ (100 sccm)
Ar diluent gas flow rate:	$1.67 \times 10^{-6} \text{ m}^3 \text{ s}^{-1}$ (100 sccm)
Nozzle diameter:	6.0 mm
Distance between nozzle and substrate:	15 mm

3. Results and Discussion

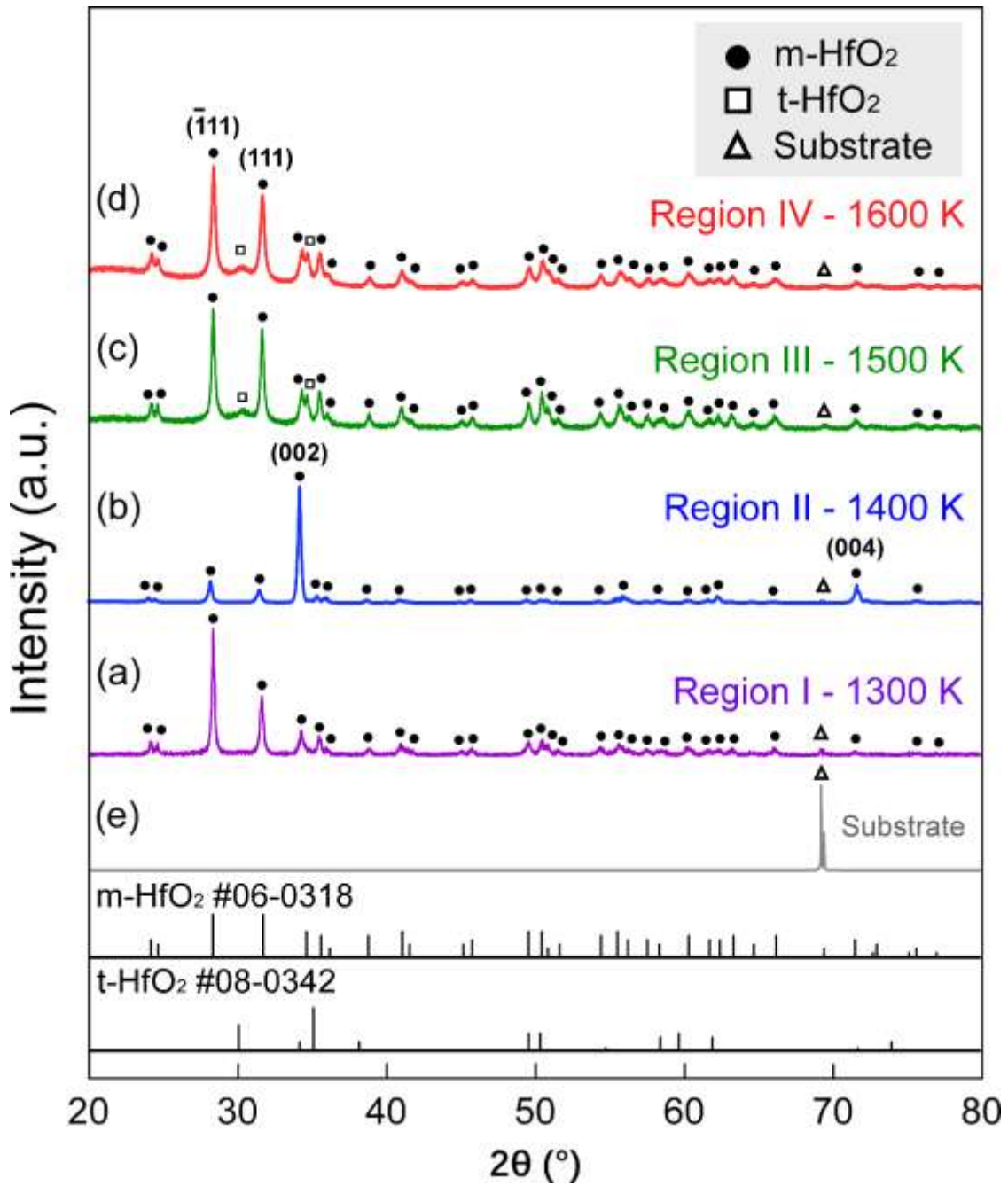


Fig. 4. μ -XRD patterns of different regions in HfO_2 film produced by the high-throughput growth process: (a) 1300K/I, (b) 1400K/II, (c) 1500K/III, (d) 1600K/IV, and (e) Si (100) substrate.

Fig. 4(a)~(d) displays the μ -XRD patterns of the 4 temperature regions in a HfO_2

film grown on Si (001) shown in Fig. 2, which were indexed with JCPDS data, No. 06-0318 (monoclinic HfO₂, P2₁/c) and No. 08-0342 (tetragonal HfO₂, P4₂/nmc). The ($\bar{1}11$) and (111) main peaks of m-HfO₂ at $2\theta = 28.3^\circ$ and 31.7° , respectively, were identified for all specimens. The patterns for Regions I (1300 K) and II (1400 K) showed no trace of t-HfO₂ peaks. At $T_{dep} = 1400$ K, m-HfO₂ exhibited a strong $\langle 002 \rangle$ orientation. The two diffraction peaks at $2\theta = 34.6^\circ$ and 72.7° corresponded to the (002) and (004) planes of m-HfO₂, respectively. The patterns for Regions III (1500 K) and IV (1600 K) exhibited two prominent peaks at $2\theta = 30.1^\circ$ and 35.1° corresponding to the ($\bar{1}11$) and (111) planes of t-HfO₂, respectively, indicating the coexistence of m- and t-HfO₂. Eq. (1) shows an approximate calculation formula that Luo *et al.* [33] developed to estimate the proportion of m-HfO₂, C_m , from μ -XRD patterns with high precision:

$$C_m \% = \frac{100}{1 + \frac{R_m}{R_t} \frac{I_t}{I_m}} \quad (1)$$

where R_m/R_t is the ratio of the standard diffraction coefficients of m- and t-HfO₂ and was calculated as 0.85 [6]. I_t/I_m is the ratio of the main-peak diffraction intensities of the two phases corresponding to the m-HfO₂ ($\bar{1}11$) and t-HfO₂ (111) planes. Using Eq. (1), the proportion of m-HfO₂ in Regions III and IV was calculated as 82% and 74%, respectively, indicating a slight increase in the proportion of t-HfO₂ grains from 1500 K to 1600 K.

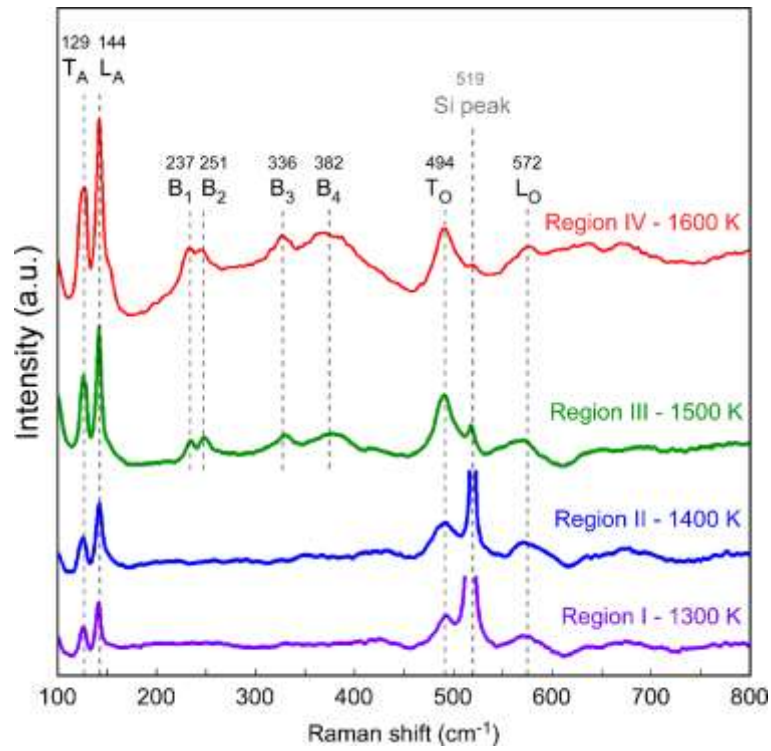


Fig. 5. Raman spectra for the four regions in the HfO₂ film.

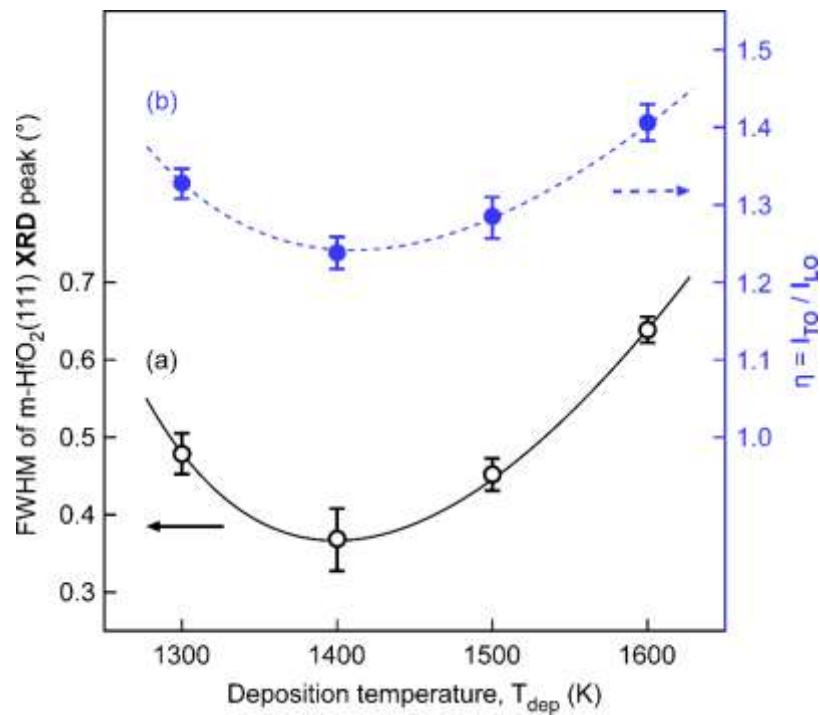


Fig. 6. (a) FWHM of the m-HfO₂(111) XRD peak and (b) intensity ratio $\eta = I_{TO} / I_{LO}$ obtained from Raman spectra of four regions with T_{dep} ranging from 1300 K to 1600

K.

Fig. 5 shows the Raman scattering spectra for the four regions with deposition temperatures of 1300-1600 K in a HfO₂ film. For Raman shifts from 100 to 800 cm⁻¹, the two characteristic peaks at ~129 cm⁻¹ and ~144 cm⁻¹ were ascribed to two acoustic phonon modes for transverse acoustic (T_A) and longitudinal acoustic (L_A) phonons of m-HfO₂ films, respectively. The intensity of the acoustic-phonon peaks increased remarkably with the film thickness [34]. Two characteristic bands appeared at approximately 494 cm⁻¹ and 572 cm⁻¹ for all samples that were ascribed to transverse optical (T_O) and longitudinal optical (L_O) phonons, respectively. For the crystal growth of m-HfO₂ films, the integral intensities of the L_O bands were expected to increase with film qualities because the L_O mode is allowed, whereas the T_O mode is forbidden. Fig. 6(b) shows the intensity ratio between T_O and L_O, η , that was used to evaluate the HfO₂ film quality. When T_{dep} increased from 1300 K to 1600 K, the lowest η was observed at 1400 K (Region II). A similar trend can be observed for the full width at half maximum (FWHM) of the m-HfO₂ (111) peaks in μ -XRD patterns shown in Fig. 6(a). Tkachev *et al.* [35] analyzed the XRD patterns and Raman spectra of polycrystalline HfO₂ films with various grain sizes and found that η for the Raman spectra decreased as the grain size increased. Hence, we inferred that the increase in the integral intensity of the HfO₂ film resulted from an increase in the proportion of large grains. For T_{dep} above 1500 K (Regions III and IV), the four broad peaks (B₁ - B₄) at ~237, ~251, ~336, and ~382 cm⁻¹ in the spectra were ascribed to the interstitial tetragonal phase that retarded the lattice vibrations at the phase boundary [36]. The integral intensity of the broad B₁ - B₄ peaks increased with the proportion of t-HfO₂, consistent with the XRD patterns. The peaks

at 519 cm^{-1} were assigned to the Si (100) substrates.

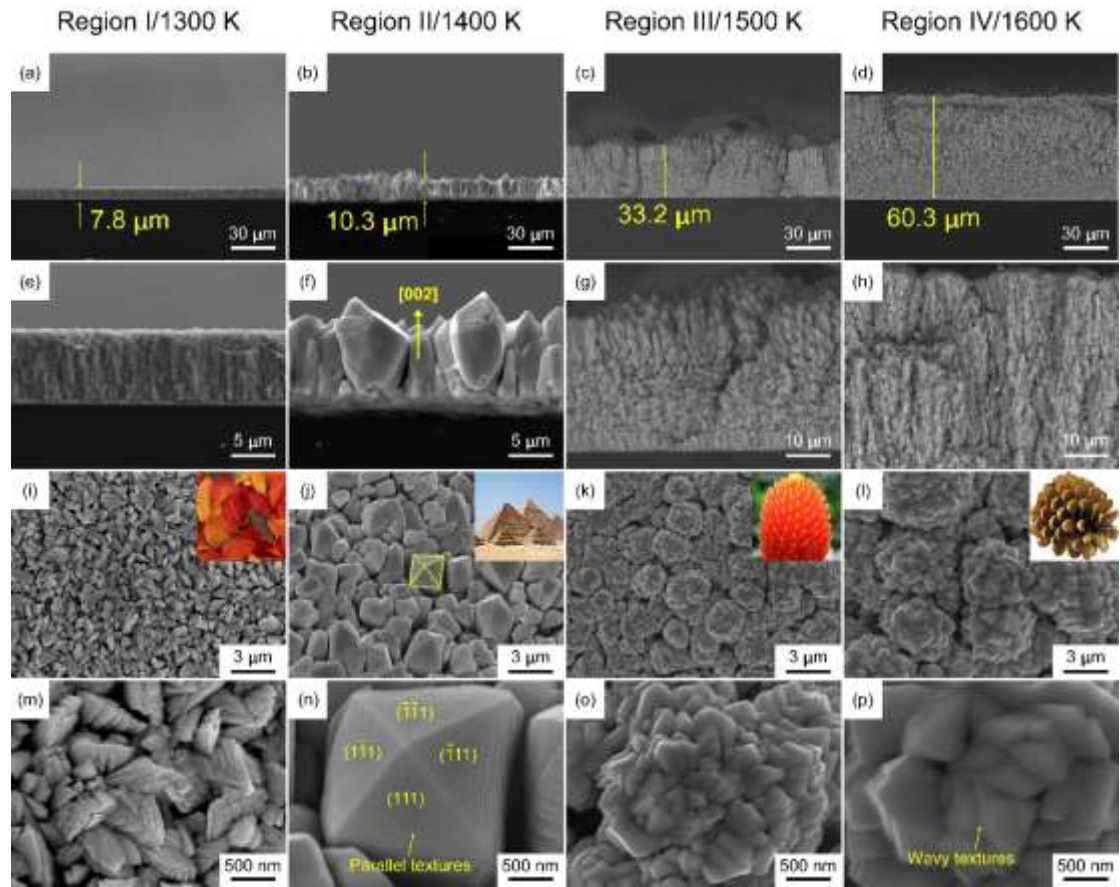


Fig. 7. SEM images of cross-sections and surfaces of HfO₂ films obtained using the high-throughput growth process with insets showing similarity of morphologies to well-known structures.

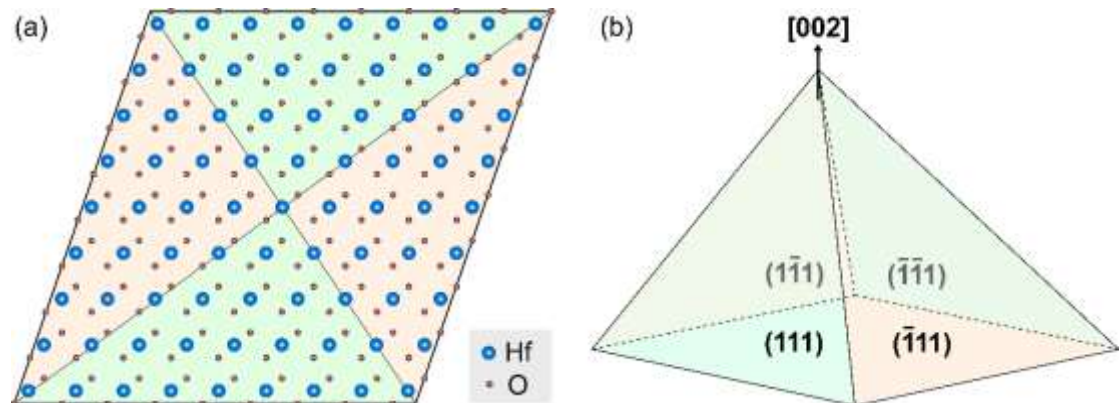


Fig. 8. Schematic model for the growth of <002>-oriented grains in Region II showing (a) atomic nodes and (b) *pyramid-like* exposed surface.

Fig. 7 shows SEM micrographs of the cross-section and surface for Regions I to IV of the HfO₂ film as T_{dep} increased from 1300 K to 1600 K. Measurements taken from the cross-sectional SEM micrographs (Fig. 7(a)~(d)) show that the thickness increased from 7.8 μm to 60.3 μm , corresponding to calculated growth rates of 46.8~362.0 $\mu\text{m}/\text{h}$. The surface SEM images show four morphologies in the as-deposited film: *leaf-like* (Fig. 7(i)), *pyramid-like* (Fig. 7(j)), *bromeliad-like* (Fig. 7(k)) and *pinecone-like* (Fig. 7(l)). The cross-sectional micrographs show the *leaf-like* structure (Region I) formed at 1300 K had a columnar microstructure. Aggregates of fine grains were arrayed in random lines on the film surface. The cross-sectional micrographs show the *pyramid-like* structure (Region II) formed at 1400 K was composed of <002>-oriented columnar grains. Fig. 7(n) shows a pyramidal faceted morphology corresponding to the (111), $(\bar{1}\bar{1}1)$, $(1\bar{1}\bar{1})$, and $(\bar{1}\bar{1}\bar{1})$ planes of m-HfO₂, with a parallel texture at the surface of (002)-oriented m-HfO₂ grains. Fig. 8(a) shows atomic nodes with a twofold rotational symmetry, which is the typical morphology of the P2₁/c space group. Javier Sanz *et al.* calculated lower surface energies for the m-HfO₂ (111) and $(\bar{1}\bar{1}1)$ planes than the (100) and (010) planes based on Born-Oppenheimer molecular dynamics (BOMD) simulations [37]. Lower surface energies usually correspond to exposed surfaces, as shown in Fig. 8(b). The cross-section micrographs show that the *bromeliad-like* structure (Region III) formed at 1500 K consists of crystal clusters. At the surface, the crystal clusters are aggregates of vertical bundles that are decorated all over with fine grains, presumably resulting from the coexistence of m- and t-HfO₂. The cross-sectional

micrographs show the *pinecone-like* structure (Region IV) formed at 1600 K exhibits a porous microstructure. The surface morphology is similar to that of Region III, except that the grain size increases from ~ 200 nm to ~ 500 nm with increasing temperature, with a wavy texture at the surface. The morphologies corresponded to XRD patterns ranging from random (Region I) to highly oriented (Region II) and back to random (Regions III and IV) with increasing temperature.

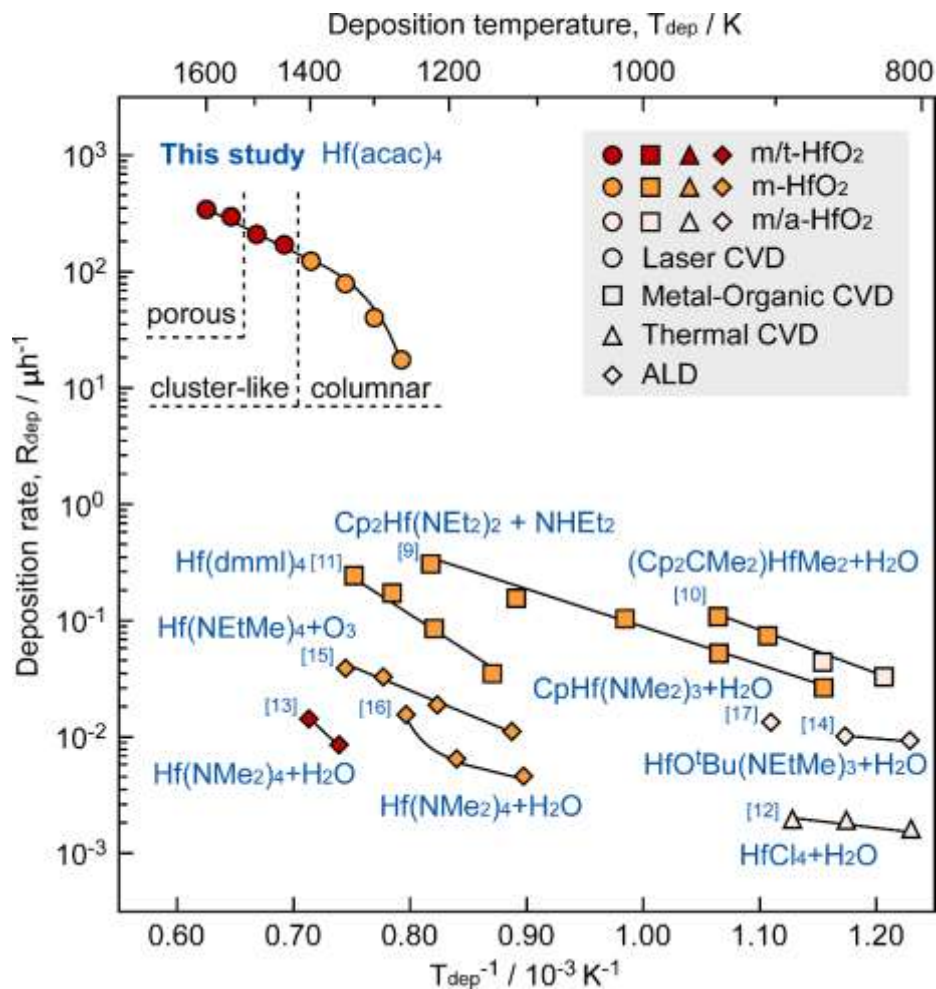


Fig. 9. Effect of T_{dep} on R_{dep} and crystal phase of HfO_2 films prepared using HT-LCVD, MOCVD, TCVD and ALD.

Fig. 9 shows a dependence of deposition rates (R_{dep}) on inverse deposition temperatures (T_{dep}^{-1}) of HfO₂ films grown using HT-LCVD, showing the presence of crystal phases (monoclinic, tetragonal or amorphous) and precursors, and the results are compared against those in the literature. To improve the measurement accuracy, the HfO₂ film was divided into eight specimens fabricated at 1250-1600 K using a single growth process. The R_{dep} of the HfO₂ film prepared by HT-LCVD reached a maximum of 362 $\mu\text{m/h}$ at $T_{\text{dep}} = 1600$ K, which was 10^2 - 10^4 times higher than that obtained using existing methods, such as MOCVD [9-11], TCVD [12] and ALD [13-17]. Using the infrared temperature-measurement program, the microstructure of the HfO₂ film was found to change from columnar to cluster-like at approximately 1420 K. A phase transition temperature above 1300 K was measured at atmospheric pressure [6]. Lin C *et al.* [38] reported that enhanced EB coatings could be prepared by increasing the microstructure transition temperature. Considering the ultrahigh melting point (3085 K) of HfO₂, EB failure could result from by the phase transition.

The Arrhenius equation was used to calculate the activation energies (E_a) of the specimens as 100-220 kJ/mol in the curved regions of the energy surface over the range of 1250–1400 K (Regions I and II) and 80 kJ/mol in the linear part of the energy surface at $T_{\text{dep}} = 1400$ –1600 K (Regions III and IV). The deposition rates in the curved regions were correlated with controlling kinetic mechanisms of deposition processes [i.e., the chemical reaction regime (CRR) or the mass transfer regime (MTR)], where the transition from CRR to MTR is normally induced by an increase in temperature [39]. Loumagne *et al.* [40] suggested that the transition from the CRR to the MTR increases

the supersaturation of the grains. In Regions I and II, the slope of the Arrhenius equation decreased from 220 kJ/mol to 100 kJ/mol, indicating a transition from the CRR to the MTR domain. A higher E_a was determined in the range of 1250–1400 K for LCVD than for other methods. Akihiko Ito *et al.* attributed this high E_a to the breakage of precursor bonds by laser phonons in LCVD [41]. Therefore, an increase in the number of active radicals over the growing surface increased R_{dep} .

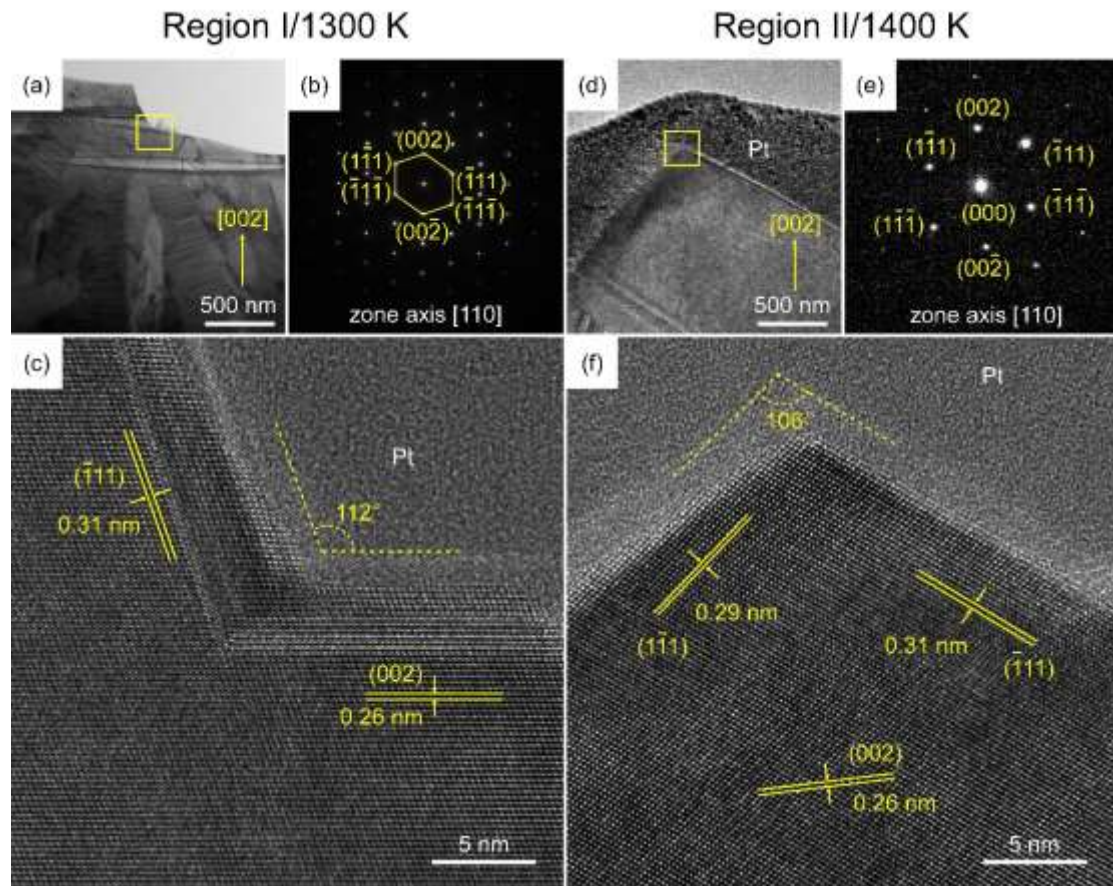


Fig. 10. Cross-section TEM images of Regions I and II in m-HfO₂.

Fig. 10 shows cross-section TEM images of the *leaf-like* and *pyramid-like* specimens. The bright-field (BF) image of Region I shows columnar grains with a variety of

orientations. The selected area electron diffraction (SAED) pattern exhibited in Fig. 10(b) was indexed to a set of well-defined (002) sites along the zone axis of [110]. Application of Vander Drift's evolutionary selection model [39] to the high-resolution (HR) TEM image revealed exposed surfaces along the $[\bar{1}11]$ or [002] directions, which explained why the fastest growing crystallographic plane overlaid the other growing planes. Komiyama *et al.* [43] developed a model for the CRR or MTR controlling mechanisms of the CVD processes by assuming Langmuir-type adsorption of the reactants. The *leaf-like* structure formed at 1300 K was associated with CRR, and R_{dep} was expressed as given in Eq. (2):

$$R_{dep} = k_r N_{hkl} V \quad (2)$$

where k_r , N_{hkl} , and V represent the reaction-limited rate coefficient, atomic density of the (hkl) plane, and molar volume of HfO₂, respectively. In a finite region, $R_{dep} \propto N_{hkl}$. The natural stacking sequence of the m-HfO₂ unit cell with P2₁/c symmetry lies along the $[\bar{1}11]$ direction, in agreement with the XRD patterns. As there was insufficient energy for the system to reach the equilibrium state at a low temperature, supersaturation of m-HfO₂ grains led to lattice distortion of the $(\bar{1}11)$ planes and a variety of orientations in Region I. The overall growth process could be considered an extension of the Stranski-Krastanov (SK) growth mode [43] for a two-dimensional (2D) thin film to a finite 3D case.

The SAED in Fig. 10(e) for Region II was indexed to a set of (002) sites along the zone axis of [110]. The HRTEM image showed exposed surfaces corresponding to the $(\bar{1}\bar{1}1)$ and $(\bar{1}11)$ planes of m-HfO₂. The distinct *pyramid-like* structure formed at 1400

K was associated with MTR, and R_{dep} was expressed using Eq. (3):

$$R_{dep} = k_s \eta_{hkl} V \quad (3)$$

where k_s and η_{hkl} represent the adsorption-limited rate coefficient and sticking probability for the (hkl) plane, respectively. For Langmuir-type adsorption, the stacking sequence transforms into the multiple-layer inclusions of other polytypes [43]. The *pyramid-like* structure was formed by the Volmer-Weber (VW) island growth mode [44] and provided many adsorption sites, making [002] the fastest growing direction. The faster-growing grains covered the slower-growing grains, such that the grains along the fastest [002] growing direction survived and dominated the entire thickness.

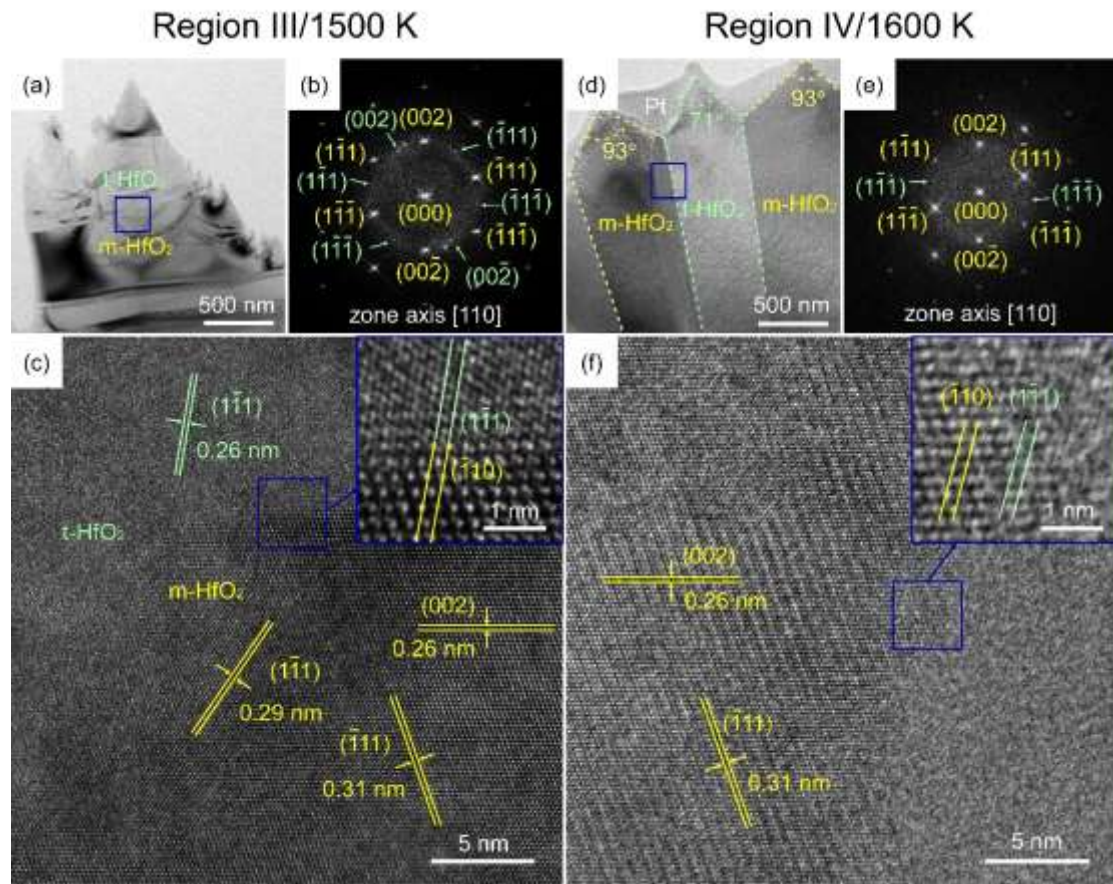


Fig. 11. Cross-section TEM images of Regions III and IV in m/t-HfO₂.

Fig. 11 shows the cross-section TEM images of the *bromeliad-like* and *pinecone-like* specimens composed of monoclinic (yellow) and tetragonal (bright green) grains. When the deposition temperature exceeded 1500 K, growth deviated from the equilibrium state again via the Volmer-Weber (VW) island growth mode [44], and the increase in the concentration of activated molecules resulted in an increase in the supersaturation of the grains. The HRTEM images showed the in-plane boundary for m-HfO₂($\bar{1}10$){111}//t-HfO₂(1 $\bar{1}1$){111}. Falkowski *et al.* found a similar structure in m/t-ZrO₂ along the O-[010]//M-[010] direction by modeling the field-induced phase transition [45]. The self-vanishing defects at the interface induced the migration of {111} planes, such that no distinct interface between the two phases of HfO₂ could be observed.

4. Conclusion

In this study, high-throughput HfO₂ films were deposited on Si (100) substrates via HT-LCVD using Hf(acac)₄ as a precursor. The maximum deposition rate of 362 $\mu\text{m/h}$ was $10^2 \sim 10^4$ times higher than that obtained using existing CVD methods. The HfO₂ films obtained using a single growth process could be divided into four regions corresponding to increasing T_{dep} from 1300 K to 1600 K, with orientations ranging from random to highly oriented and back to random. The *leaf-like* region formed at 1300 K was associated with CRR and was a nonequilibrium state that could be modeled by extending the Stranski-Krastanov growth mode on a two-dimensional (2D) thin film to a finite 3D case. The columnar grains in the *pyramid-like* region formed at a T_{dep} of 1400 K exhibited a strong $\langle 002 \rangle$ orientation that was associated with the transition

from CRR to MTR. In Region II, a Volmer-Weber growth mode resulted in faster-growing grains covering slower-growing grains, whereby grains survived along the fastest growing direction. As the temperature rose to 1500 K, the concentration of activated molecules increased, resulting in an increase in the supersaturation of the grains. Regions III (*bromeliad-like*, 1500 K) and IV (*pinecone-like*, 1600 K) consisted of coexisting monoclinic and tetragonal phases, with an in-plane boundary for m-HfO₂ ($\bar{1}10$) {111} // t-HfO₂ ($1\bar{1}1$) {111}.

Conflict of interest

The authors declare that they have no conflict of interest.

Acknowledgement

This work was supported by the National Natural Science Foundation of China (Nos. 51861145306, 51872212 and 51972244), and the 111 Project (B13035). It was also supported by the International Science & Technology Cooperation Program of China (2018YFE0103600), the Technological Innovation of Hubei Province, China (2019AAA030). It was also supported by the Key Area Research and Development Program of Guangdong Province (2019B121204001, 2020B010181001), the Chaozhou Science and Technology Project (2019PT01), the Self-innovation Research Funding Project of Hanjiang Laboratory (HJL202012A001, HJL202012A002, HJL202012A003) and the Major Science and Technology Project in Zhongshan City, Guangdong Province (2019AG029).

References

- [1] Li C, Belkin D, Li Y, *et al.* Efficient and self-adaptive in-situ learning in

- multilayer memristor neural networks. *Nat Commun* 2018, **9**: 2385.
- [2] Dorvel BR, Reddy B, Go J, *et al.* Silicon Nanowires with High-k Hafnium Oxide Dielectrics for Sensitive Detection of Small Nucleic Acid Oligomers. *Acs Nano* 2012, **6**: 6150-6164.
- [3] Huang Y, Wan C. Controllable fabrication and multifunctional applications of graphene/ceramic composites. *J Adv Ceram* 2020, **9**: 271-291.
- [4] Oh I, Tanskanen J, Jung H, *et al.* Nucleation and Growth of the HfO₂ Dielectric Layer for Graphene-Based Devices. *Chem Mater* 2015, **27**: 5868-5877.
- [5] Matsumoto K, Itoh Y, Kameda T. EB-PVD process and thermal properties of hafnia-based thermal barrier coating. *Sci Technol Adv Mat* 2003, **4**: 153-158.
- [6] Choi JH, Mao Y, Chang JP. Development of hafnium based high-k materials—A review. *Mat Sci Eng R* 2011, **72**: 97-136.
- [7] Brewer JC, Walters RJ, Bell LD, *et al.* Determination of energy barrier profiles for high-k dielectric materials utilizing bias-dependent internal photoemission. *Appl Phys Lett* 2004, **85**: 4133-4135.
- [8] Bohr MT, Chau RS, Ghani T, *et al.* The high-k solution. *Ieee Spectr* 2007, **44**: 29-35.
- [9] Carta G, El Habra N, Rossetto G, *et al.* Growth of hafnium dioxide thin films by MOCVD using a new series of cyclopentadienyl hafnium compounds. *Chem Vapor Depos* 2007, **13**: 626-632.
- [10] Black K, Aspinall HC, Jones AC, *et al.* Deposition of ZrO₂ and HfO₂ thin films by liquid injection MOCVD and ALD using ansa-metallocene zirconium and

- hafnium precursors. *J Mater Chem* 2008, **18**: 4561-4571.
- [11] Park T, Kim J, Jang J, *et al.* Improved Growth and Electrical Properties of Atomic-Layer-Deposited Metal-Oxide Film by Discrete Feeding Method of Metal Precursor. *Chem Mater* 2011, **23**: 1654-1658.
- [12] Chung J, Tak YJ, Kim W-G, *et al.* Low-temperature fabrication of solution-processed hafnium oxide gate insulator films using a thermally purified solution process. *J Mater Chem C* 2018, **6**: 4928-4935.
- [13] Jud E, Tang M, Chiang YM. Stability of HfO₂/SiO_x/Si surficial films at ultralow oxygen activity. *J Appl Phys* 2008, **103**: 114108.
- [14] Seo M, Min Y-S, Kim SK, *et al.* Atomic layer deposition of hafnium oxide from tert-butoxytris(ethylmethylamido)hafnium and ozone: rapid growth, high density and thermal stability. *J Mater Chem* 2008, **18**: 4324-4331.
- [15] Lee SY, Kim HK, Lee JH, *et al.* Effects of O₃ and H₂O as oxygen sources on the atomic layer deposition of HfO₂ gate dielectrics at different deposition temperatures. *J Mater Chem C* 2014, **2**: 2558-2568.
- [16] Oh I, Park B, Seo S, *et al.* Comparative study of the growth characteristics and electrical properties of atomic-layer-deposited HfO₂ films obtained from metal halide and amide precursors. *J Mater Chem C* 2018, **6**: 7367-7376.
- [17] Park S, Park B, Yoon H, *et al.* Comparative study on atomic layer deposition of HfO₂ via substitution of ligand structure with cyclopentadiene. *J Mater Chem C* 2020, **8**: 1344-1352.
- [18] Acton O, Ting G, Ma H, *et al.* Pi-sigma-Phosphonic Acid Organic

- Monolayer/Sol-Gel Hafnium Oxide Hybrid Dielectrics for Low-Voltage Organic Transistors. *Adv Mater* 2008, **20**: 3697-3701.
- [19] Acton O, Dubey M, Weidner T, *et al.* Simultaneous Modification of Bottom-Contact Electrode and Dielectric Surfaces for Organic Thin-Film Transistors Through Single-Component Spin-Cast Monolayers. *Adv Funct Mater* 2011, **21**: 1476-1488.
- [20] Zakaria MB, Nagata T, Chikyow T. Mesostructured HfO₂/Al₂O₃ Composite Thin Films with Reduced Leakage Current for Ion-Conducting Devices. *ACS Omega* 2019, **4**: 14680-14687.
- [21] Verrelli E, Tsoukalas D. Investigation of the gate oxide leakage current of low temperature formed hafnium oxide films. *J Appl Phys* 2013, **113**: 114103.
- [22] Wang Y, Wang H, Ye C, *et al.* Interfacial reaction and electrical properties of HfO₂ film gate dielectric prepared by pulsed laser deposition in nitrogen: role of rapid thermal annealing and gate electrode. *ACS Appl Mater Inter* 2011, **3**: 3813-3818.
- [23] Zhang S, Tu R, Goto T, *et al.* High-Speed Epitaxial Growth of β -SiC Film on Si(111) Single Crystal by Laser Chemical Vapor Deposition. *J Am Ceram Soc* 2012, **95**: 2782-2784.
- [24] Zhang S, Xu Q, Tu R, *et al.* High-Speed Preparation of $\langle 111 \rangle$ - and $\langle 110 \rangle$ -Oriented β -SiC Films by Laser Chemical Vapor Deposition. *J Am Ceram Soc* 2014, **97**: 952-958.
- [25] Yu S, Tu R, Goto T. Preparation of SiOC nanocomposite films by laser chemical

- vapor deposition. *J Eur Ceram Soc* 2016, **36**: 403-409.
- [26] You Y, Ito A, Tu R, *et al.* Effects of laser power on the growth of polycrystalline AlN films by laser chemical vapor deposition method. *Surf Coat Tech* 2013, **232**: 1-5.
- [27] Chi C, Katsui H, Tu R, *et al.* Preparation of Li–Al–O films by laser chemical vapor deposition. *Mater Chem Phys* 2014, **143**: 1338-1343.
- [28] Guo D, Ju Y, Ito A, *et al.* Dielectric properties of BaTi₂O₅ thick films prepared on Pt-coated MgO(110) single-crystal substrate by laser chemical vapor deposition. *Ceram Int* 2016, **42**: 11464-11467.
- [29] Wang T, Wang K, Tu R, *et al.* Thickness dependence of structure and superconductivity of the SmBa₂Cu₃O₇ film by laser CVD. *RSC Adv* 2017, **7**: 56166-56172.
- [30] Zhang S, Xu Q, Tu R, *et al.* Growth Mechanism and Defects of <111>-Oriented β-SiC Films Deposited by Laser Chemical Vapor Deposition. *J Am Ceram Soc* 2015, **98**: 236-241.
- [31] Zhang Z, Guo Y, Lu H, *et al.* Hybrid band offset calculation for heterojunction interfaces between disparate semiconductors. *Appl Phys Lett* 2020, **116**: 131602.
- [32] Zhang C, Fan Y, Zhao J, *et al.* Corrosion resistance of non-stoichiometric gadolinium zirconate fabricated by laser-enhanced chemical vapor deposition. *J Adv Ceram* 2021, **10**: 520-528.
- [33] Luo X, Demkov AA, Triyoso D, *et al.* Combined experimental and theoretical study of thin hafnia films. *Phys Rev B* 2008, **78**: 245314.

- [34] Govindaraj R, Sundar CS, Kesavamoorthy R. Atomic scale study of oxidation of hafnium: Formation of hafnium core and oxide shell. *J Appl Phys* 2006, **100**: 084318.
- [35] Tkachev SN, Manghnani MH, Nilisk A, *et al.* Micro-Raman spectroscopy and X-ray diffraction studies of atomic-layer-deposited ZrO₂ and HfO₂ thin films. *J Mater Sci* 2005, **40**: 4293-4298.
- [36] Ristic D, Ivanda M, Furic K, *et al.* Raman scattering on quadrupolar vibrational modes of spherical nanoparticles. *J Appl Phys* 2008, **104**: 073519.
- [37] Mukhopadhyay AB, Musgrave CB, Sanz JF. Atomic layer deposition of hafnium oxide from hafnium chloride and water. *J Am Chem Soc* 2008, **130**: 11996-12006.
- [38] Chen L, Feng J. Influence of HfO₂ alloying effect on microstructure and thermal conductivity of HoTaO₄ ceramics. *J Adv Ceram* 2019, **8**: 537-544.
- [39] Tu R, Zheng D, Sun Q, *et al.* Ultra-Fast Fabrication of <110>-Oriented β-SiC Wafers by Halide CVD. *J Am Ceram Soc* 2016, **99**: 84-88.
- [40] Loumagne F, Langlais F, Naslain R, *et al.* Physicochemical properties of SiC-based ceramics deposited by low pressure chemical vapor deposition from CH₃SiCl₃H₂. *Thin Solid Films* 1995, **254**: 75-82.
- [41] Matsumoto S, Kaneda Y, Ito A. Highly self-oriented growth of (020) and (002) monoclinic HfO₂ thick films using laser chemical vapor deposition. *Ceram Int* 2020, **46**: 1810-1815.
- [42] Nishioka K, Mizutani N, Komiyama H. A Model for Predicting Preferential

Orientation of Chemical-Vapor-Deposited Films. *J Electrochem Soc* 2000, **147**: 1440-1442.

- [43] Oh MH, Cho MG, Chung DY, *et al.* Design and synthesis of multigrain nanocrystals via geometric misfit strain. *Nature* 2020, **577**: 359-+.
- [44] Kooi BJ, Wuttig M. Chalcogenides by Design: Functionality through Metavalent Bonding and Confinement. *Adv Mater* 2020, **32**: 1908302.
- [45] Falkowski M, Kersch A. Optimizing the Piezoelectric Strain in ZrO₂- and HfO₂-Based Incipient Ferroelectrics for Thin-Film Applications: An Ab Initio Dopant Screening Study. *Acs Appl Mater Inter* 2020, **12**: 32915-32924.